Journal of Materials Science: Materials in Electronics (2019) 30:7940–7949
https://doi.org/10.1007/s10854-019-01115-4

Facile synthesis of controllable carbonate-doped TiO_2 microspheres for visible light photocatalytic applications

Bingkun Liu[1] · Xiaole Han[1] · Yajun Wu[1] · Yongfei Xue[1] · Hengzhen Shi[1]

Received: 18 December 2018 / Accepted: 11 March 2019 / Published online: 15 March 2019

Abstract
Mesoporous carbonate-doped TiO_2 microspheres were prepared by a facile solvothermal route combining a low-temperature annealing process. XPS, TG, and FTIR analysis revealed the presence of carbonate species on TiO_2 surface, which extended the optical absorption of the TiO_2 microspheres to the visible region. The carbonate-doped T200 microspheres exhibited much higher photocatalytic degradation of MO activity compared with non-doped T400 microspheres under visible light illumination. By adjusting initial titanium precursor concentration and reaction time, the best photocatalytic performance of carbonate-doped T200 microspheres was obtained. In addition, carbonate-doped T200 microspheres also displayed good photocatalytic disinfection efficiency towards *Escherichia coli* under visible light exposure. Our study revealed that the carbonate-doped TiO_2 microspheres would be applied in the water treatment for the degradation of organic pollutants and disinfection of bacteria.

1 Introduction

As a "green" technology, semiconductor photocatalysis based on solar energy utilization has attracted increasing attentions by removing organic pollutants and pathogenic bacteria from wastewater [1–3]. Of the well-known semiconductor materials, TiO_2 has proved to be effective photocatalysts in plenty of environmental application fields owing to its low cost, nontoxicity, long-term stability and high photocatalytic efficiency [4–6]. But the widespread usage of TiO_2 is greatly hindered by its large band gap and fast recombination of photo-induced electron–hole pairs. Much effort has been attempted to enhance the photocatalytic property of TiO_2, including noble metals deposition [7], metal or nonmetal elements doping [8], organic dyes sensitization [9], and other semiconductors coupling [10].

For the decades, it has been demonstrated that carbon-doped TiO_2 was an effective way to induce visible light absorption through narrowing the TiO_2 band gap [11–14]. But the preparation methods usually needed high temperature, which could damage the porous TiO_2 nanostructure [12, 14]. Recently, carbonate-doped TiO_2 photocatalysts synthesized at low temperature have been reported to improve visible light induced photocatalytic activities [15–20]. Liu et al. first developed a simple solvothermal route for preparing carbonate-doped TiO_2 microspheres, which displayed very high photocatalytic activity as compared with other TiO_2 photocatalysts [15]. Liu et al. demonstrated that carbonate doping can narrow the TiO_2 bandgap and also act as photosensitizer to promote the charge carriers' separation [16]. However, to our best knowledge, the influences of synthesis parameters on the morphology, structure and photocatalytic activity of carbonate-doped TiO_2 microspheres have not been studied systematically. In addition, their antibacterial activity was still unknown under the exposure of visible light.

In this work, we synthesized carbonate-doped mesoporous TiO_2 microspheres using a facile solvothermal method and subsequent low-temperature annealing treatment. Then the carbonate-doped TiO_2 microspheres was utilized for photodegradation of methyl orange (MO) and disinfection of *Escherichia coli* (*E. coli*) under visible light illumination. The effects of various synthesis parameters (initial titanium precursor concentration and the reaction time) on the morphology, structure, optical and photocatalytic properties

Electronic supplementary material The online version of this article (https://doi.org/10.1007/s10854-019-01115-4) contains supplementary material, which is available to authorized users.

✉ Bingkun Liu
liubk2015@zzuli.edu.cn

[1] School of Material and Chemical Engineering, Zhengzhou University of Light Industry, Zhengzhou 450002, People's Republic of China

were investigated. Finally, the possible enhanced visible light photocatalytic mechanism with carbonate-doped TiO_2 microspheres was proposed.

2 Experimental section

2.1 Synthesis of photocatalysts

Firstly, TiO_2 microspheres were prepared through a facile solvothermal process. 2 mL of titanium isopropoxide (TIP, Aldrich Chemical Reagent Co., Ltd) was added into 60 mL of acetone (≥ 99.5%, Sinopharm Chemical Reagent Co.,Ltd). After stirring vigorously for 5 min, the mixture was transferred to 100 mL Teflon-lined stainless-steel autoclave and then reacted at 200 °C for 4 h. After cooling down to room temperature, the precipitate was collected by centrifugation, washed with deionized water and acetone for several times, and dried under vacuum at 60 °C. At last, the carbonate-doped TiO_2 microspheres were achieved in subsequent 2 h calcination at 200 °C in a furnace, which was denoted as T200. For comparison, the non-doped TiO_2 microspheres were prepared by heating at 400 °C, denoted as T400.

2.2 Characterization

X-ray diffraction (XRD) patterns were obtained on Rigaku D/Max-2500 diffractometer with Cu Kα radiation. The morphologies were observed by field emission scanning electron microscopy (FESEM, JSM-7001F) and transmission electron microscopy (TEM, JEM-2100). X-ray photoelectron spectroscopy (XPS) was recorded on ESCALAB 250Xi photoelectron spectrometer with Al Kα X-ray source. Thermogravimetric (TG) analysis was conducted on a Perkin-Elmer Diamond TG/DTA thermal analyzer with a heating rate of 10 °C min^{-1}. Fourier transform infrared (FTIR) spectra were measured by a Nicolet 5700 spectroscope. The Brunauer–Emmett–Teller (BET) surface area and Barrett–Joyner–Helenda (BJH) pore size distribution were carried out using N_2 adsorption–desorption isotherms. UV–Vis diffuse reflection spectroscopy (DRS) was recorded on Hitachi U-3900H spectrometer with $BaSO_4$ as the reference. Steady state photoluminescence (PL) and time-resolved photoluminescence decay (TRPL) measurements were carried out on FLS 980 fluorescence spectrometer (Edinburgh Instrument).

2.3 Photodegradation experiment

The photodegradation performance was evaluated by removing methyl orange (MO, 10 mg L^{-1}) under visible light from a 300 W Xe lamp with a UV-cutoff filter (λ > 400 nm). Before irradiation, 20 mg of photocatalyst was dispersed in 40 mL of MO solution and then stirred in dark for 60 min to achieve adsorption–desorption equilibrium. When the visible light was on, an aliquot of the solution was taken from the mixture at certain time. After removing the photocatalyst by centrifugation, the concentration was analyzed by measuring the maximum absorbance using a Hitachi U-3900H spectrophotometer at 463 nm for MO. Meanwhile, active specie trapping experiments were carried out to study the photocatalytic degradation mechanism. The procedure was similar to the photodegradation experiment except that the radical scavengers were added to the reaction system.

2.4 Antibacterial experiment

The culture of *E. coli* cells was previously reported in our research group [21]. The photocatalytic antibacterial experiment was irradiated by a 300 W Xe lamp with a 400 nm UV-cutoff filter and the light intensity was fixed at *ca*. 30 mW/cm^2. When the light turned on, 0.1 mL aliquot of the cell suspension were collected at given time intervals. After diluting with PBS buffer solution (pH ~ 7), the 0.1 mL of sample were quickly spread on nutrient agar and then put them in an incubator at 37 °C for 24 h. Finally, the number of viable cells was counted in terms of colony-forming units (CFU). All experiments were performed in triplicate and the average value were given. To make comparison, light control and dark control experiments were also conducted. The active specie trapping experiments were also performed by adding various scavengers to the photocatalytic disinfection system.

3 Results and discussion

Figure 1a shows the XRD patterns of the as prepared T200 and T400 samples. It can be seen that all the diffraction peaks were ascribed to anatase phase of TiO_2 (JCPDS No. 21-1272). Moreover, the intensity of anatase peaks increased with the calcining temperature. Using Scherrer equation [15, 19], the mean nanocrystallite sizes were calculated to be 10.2 nm and 14.6 nm for T200 and T400, respectively. The results suggested higher calcination temperature brings up larger crystallite size and better crystallinity.

FTIR analysis was conducted to reveal the bonding characteristics in T200 and T400 samples, as shown in Fig. 1b. For both samples, the absorption bands in the range of 500–800 cm^{-1} were derived from stretching mode of O–Ti–O bond [22]. The bands at 3000–3500 cm^{-1} and 1633 cm^{-1} were caused by the surface hydroxyl stretching and bending vibration [20, 23]. The peak at around 2258 cm^{-1} is attributed to the carbon dioxide in the air [20]. In addition, the T200 sample displayed additional peaks centering at 1351 cm^{-1}, 1440 cm^{-1} and 1535 cm^{-1}

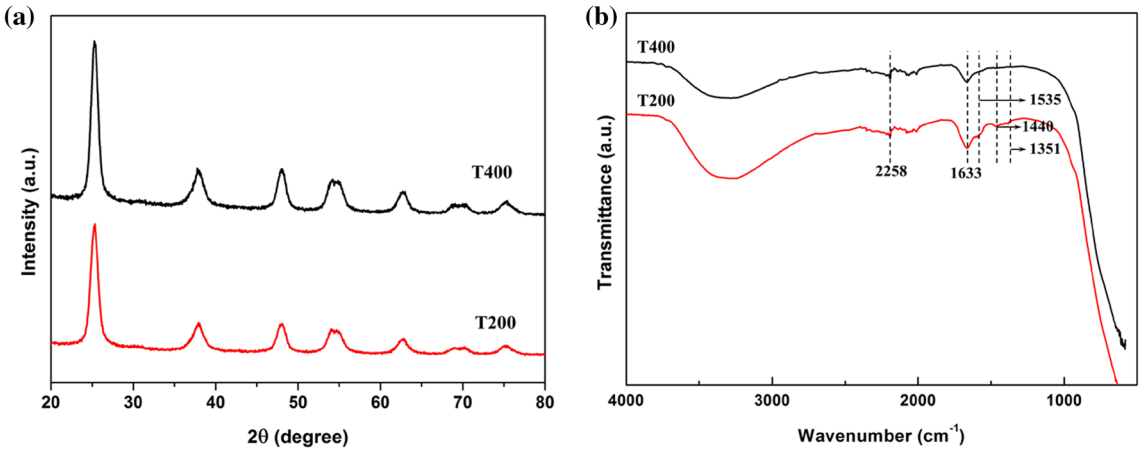

Fig. 1 **a** XRD patterns and **b** FTIR spectra of as-prepared T200 and T400 samples

compared with T400 sample, which came from the stretching vibrations of COO^- and carbonate, respectively [24, 25]. When the calcinations temperature was up to 400 °C, the T400 sample had no obvious characteristic peaks of carbonate groups, implying that the high temperature resulted in complete decomposition of the carbonate-like species on the TiO_2 surface. At lower temperature, the carbonate species would not be completely removed, which has been confirmed by the TG analysis (Fig. S1). The results demonstrated that the carbonate species have been successfully introduced into T200 sample via a low-temperature method.

XPS was applied to study the chemical states of carbonate dopants in T200 sample. As shown in Fig. 2a, there were three fitting peaks at 284.5, 286.2, and 288.5 eV in the C 1s XPS spectrum. The major peak at 284.5 eV was attributed to the reference carbon, while the other two peaks at 286.2 and 288.5 eV originated from C–O and C=O in the carbonate species [15, 17, 20]. Moreover, the peak at around 282.0 eV from Ti–C bond was not found, suggesting that C was not substituted O in the TiO_2 lattice [26]. In the O 1s XPS spectrum of T200 (Fig. 2b), the peaks at 529.8 and 531.5 eV were indexed to lattice oxygen and C=O of carbonate dopants, respectively [18]. And the peak at 532.6 eV was caused by surface hydroxyl group [16, 27]. Thus, both C 1s and O 1s XPS spectra further confirmed the presence of carbonates on the surface of TiO_2.

To investigate the morphology of TiO_2 samples, SEM and TEM images have been taken and shown in Fig. 3. Both of T200 and T400 samples are spherical with diameters in the range of 500–1000 nm, and composed of numerous small nanocrystallites in the spheres. From the HRTEM image of Fig. 3c, the mean crystallite size in T200 microspheres was around 10 nm. With higher calcination temperature, the nanocrystallite size in T400 microspheres was increased to 15–20 nm and also displayed good crystallinity. Figure 3f shows the HRTEM image of T400 microspheres. It revealed a well-defined crystallinity

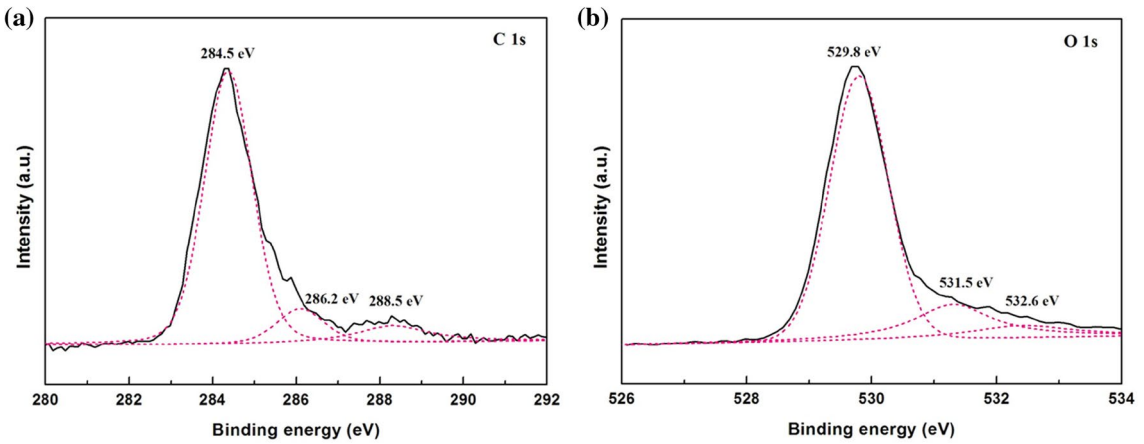

Fig. 2 **a** C 1s and **b** O 1s high resolution XPS spectra of T200 samples

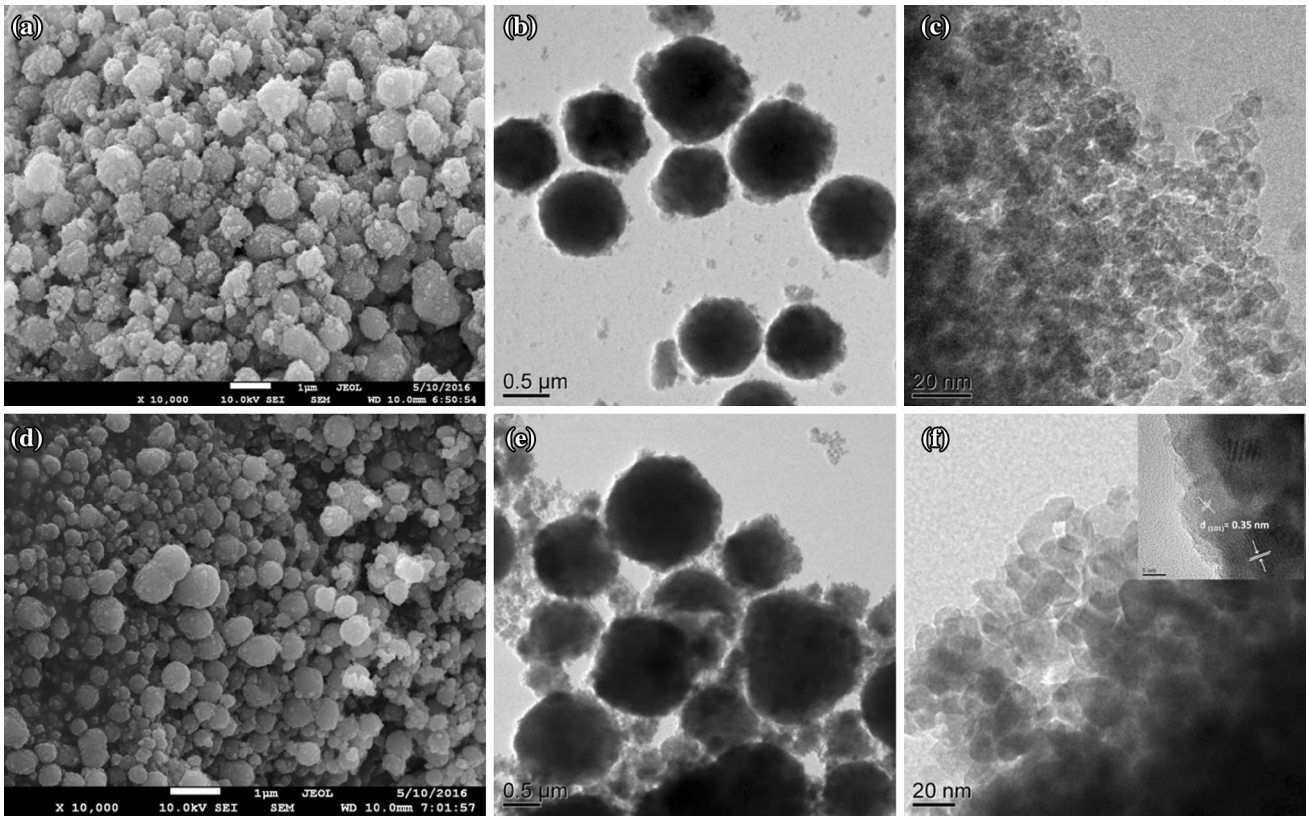

Fig. 3 FESEM, TEM and HRTEM images of T200 and T400 samples: **a**–**c** T200; **d**–**f** T400

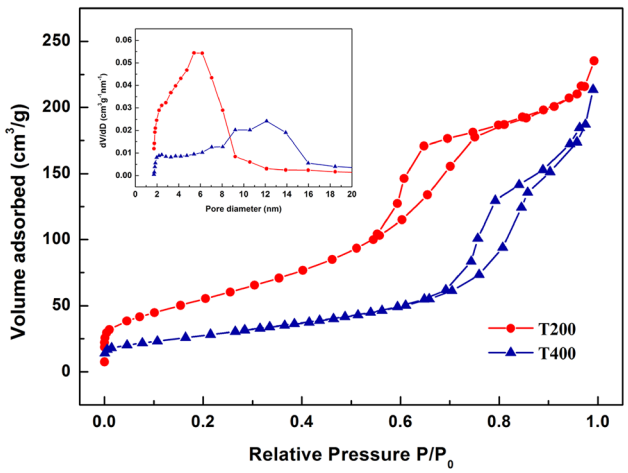

Fig. 4 N_2 adsorption–desorption isotherms of T200 and T400 samples. The inset shows the corresponding pore size distribution

of TiO_2 with fringes spacing of 0.35 nm, corresponding to the (101) planes of tetragonal anatase.

Nitrogen adsorption–desorption isotherms were tested to determine the specific surface areas and pore size distributions of T200 and T400 samples. As shown in Fig. 4, it could be seen that both samples exhibited obvious hysteresis loops, implying the existence of the pores among aggregated particles [28]. From the pore distribution curves (inset), it revealed that the mean pore sizes were 6 nm and 12 nm for T200 and T400 microspheres, implying their mesoporous structure. The relatively large pores in T400 microspheres are caused by the loss of surface carbonate-like groups on TiO_2 at the high temperature. In addition, the T200 microspheres had relatively higher surface area (207.47 $m^2\ g^{-1}$) than that of T400 microspheres (100.48 $m^2\ g^{-1}$), which should be related to the smaller crystalline size at low temperature.

UV–Vis DRS was employed to investigated the light absorption properties of the samples. As can be seen from Fig. 5a, it was found that the T200 sample presented the brown color and exhibited stronger absorption in the visible region of 400–800 nm. After heat-treatment at 400 °C, the color of T400 sample turned to white and showed little absorption in visible-light region beyond 400 nm. This was caused by the complete removal of carbonate-like species on TiO_2 surface at high temperature. According to the Tauc plots [29, 30], we further calculated the band gaps of the samples(Fig. 5b). The obtained band gap values were 2.95 eV for T200 and 3.18 eV for T400, respectively. The narrowing of band gap of T200 was attributed to the carbonate doping in the TiO_2 bandgap [17]. In the meantime, the

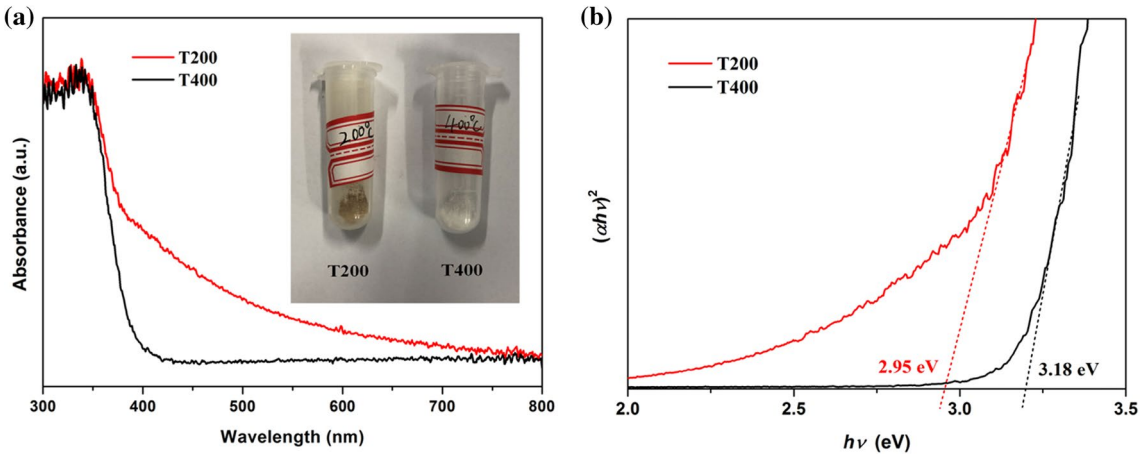

Fig. 5 **a** UV–Vis diffuse reflectance spectra of T200 and T400 samples; **b** Tauc plots for band gap determination of T200 and T400samples

carbonate species on the surface of TiO_2 can serve as photosensitizer and extend absorption band tails to 700 nm [16]. The results imply that carbonate-doped T200 microspheres were expected to improve the photocatalytic activity in the visible light region.

MO photodegradation was used to study the photocatalytic activity of samples under visible light illumination. Figure 6a shows the changes in the relative MO concentrations in the dark and under visible light irradiation. The adsorption curves in the dark indicated that the adsorption

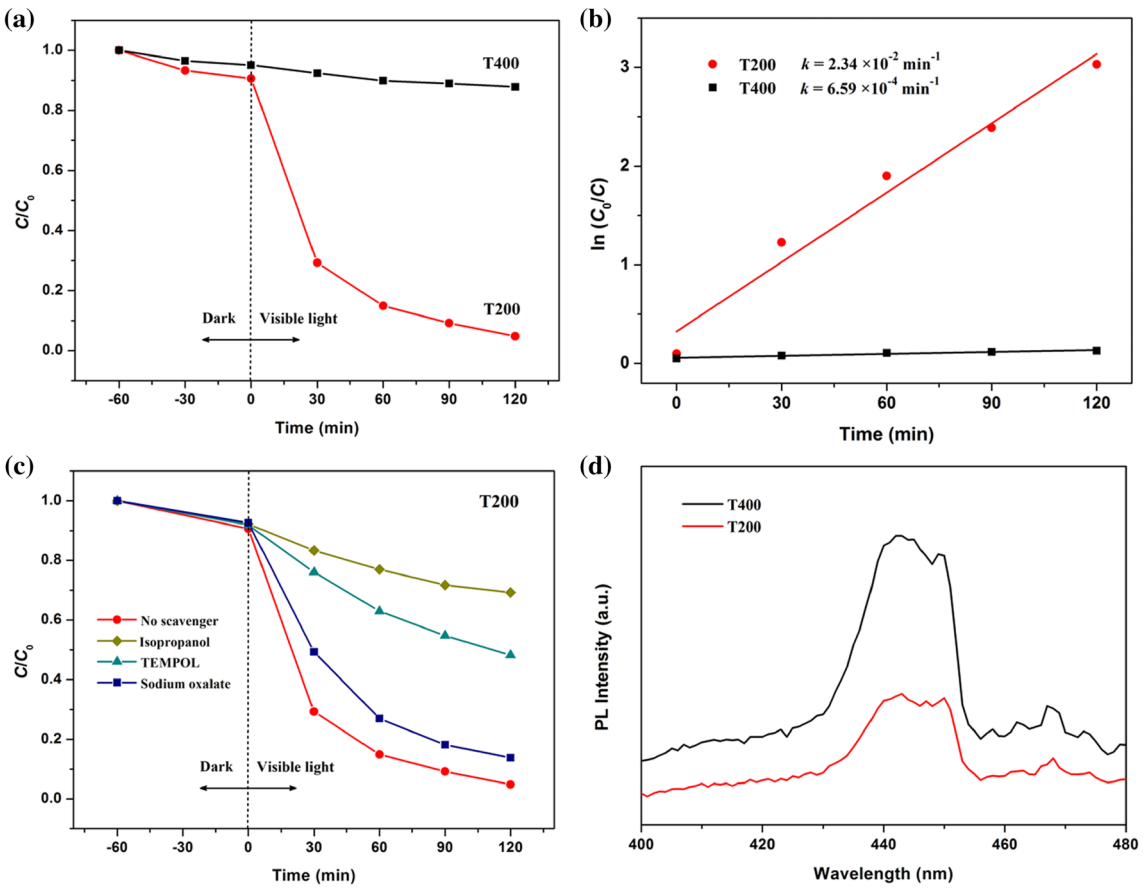

Fig. 6 **a** Photocatalytic degradation of MO and **b** corresponding pseudo first-order plots over the T200 and T400 samples; **c** trapping experiments for the degradation of MO over T200 sample; **d** photoluminescence spectra of T200 and T400 samples

process could reach equilibrium after 60 min for T200 and T400 samples. In the photodegradation process, carbonate-doped T200 sample exhibited much higher photodegradation activity as compared with T400, and MO could be completely removed after 120 min visible light exposure. Figure 6b shows the pseudo-first-order kinetics of the photocatalytic degradation reaction. The rate constant of T200 was 0.0234 min^{-1}, which was about 35.5 times higher than that of T400 microspheres (6.59×10^{-4} min^{-1}).

To investigate the photodegradation mechanism, main active species were identified by trapping experiments over T200 sample. Isopropanol, 4-hydroxy-2,2,6,6-tetramethylpiperidinyloxy (TEMPOL) and sodium oxalate were selected as the ·OH, $\cdot O_2^-$ and h^+ scavengers, respectively. As shown in Fig. 6c, after the addition of isopropanol and TEMPOL, the degradation efficiency of T200 decreased greatly, indicating the leading role of ·OH and $\cdot O_2^-$ in the photocatalytic reaction process. In contrast, little efficiency reduction with the addition of sodium oxalate implied that h^+ was not the predominant active species.

Photoluminescence (PL) spectra were carried out to study the recombination process of the photo-generated charge carriers. Figure 6d presented the PL spectra of T200 and T400 with the excitation wavelength of 280 nm. Compared with T400, the PL intensity of T200 revealed a significant decrease, which was mainly ascribed to the efficient charge carrier transfer and reduced recombination in T200 sample. To gain more understanding of this phenomenon, time-resolved PL spectra were also investigated (Fig. S2). By the bi-exponential fitting, the average PL lifetimes of T400 and T200 were calculated. It revealed that T200 (8.33 ns) had longer PL lifetime than T400 sample (6.93 ns), indicating that the separation efficiency of photogenerated charge carriers was increased in T200 sample, which was beneficial for the photocatalytic performances.

To explore the effects of synthesis parameters on morphology, optical and photocatalytic property, a set of experiments were conducted by varying titanium precursor concentration and solvothermal time. Figure 7 shows FESEM images and XRD patterns of T200 microspheres prepared with 1 mL, 2 mL and 4 mL of titanium isopropoxide (TIP).

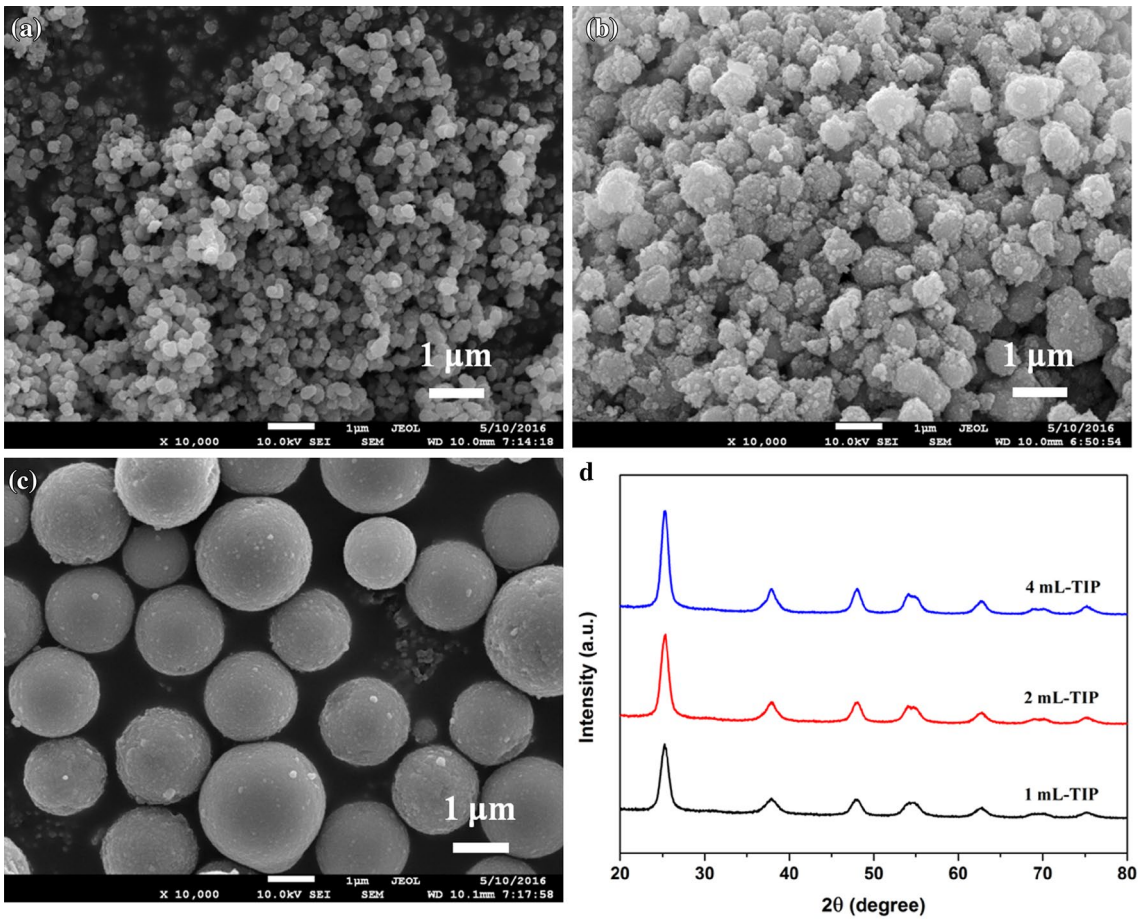

Fig. 7 FESEM images of T200 microspheres prepared with: **a** 1 mL, **b** 2 mL and **c** 4 mL of titanium isopropoxide; **d** XRD patterns of the above samples

At low TIP concentration (1 mL of TIP in 60 mL of acetone), the size of T200 microspheres was about 200 nm. With increasing TIP concentrations, the mean size of T200 microspheres dramatically increased. When the TIP precursor was increased to 4 mL, the obtained microspheres possessed a large diameter of 3 μm. XRD patterns revealed that all the T200 microspheres were anatase phase and their diffraction peak intensities gradually enhanced with the increase of TIP concentrations.

Figure 8a displays UV–Vis DRS of T200 microspheres prepared with various TIP concentrations. As can be seen, all the T200 microspheres exhibited improved optical absorptions in the visible light region and gradually enhanced with the increase of TIP concentrations. In the photodegradation experiments (Fig. 8b), all the as-prepared T200 microspheres displayed better visible light photocatalytic activity than T400 microspheres. Among them, the T200 microspheres prepared with 2 mL TIP precursor showed the highest photodegradation efficiency. Although TiO_2-4 mL microspheres presented stronger visible light absorption, the decreased surface area and overmuch carbonate species had adverse effects on the photocatalytic activity [31].

Figure 9 shows FESEM images and XRD patterns of T200 prepared with various solvothermal reaction time. When the reaction time was 2 h, the average diameter of the microspheres was 1 μm. As reaction time gradually increased, the microspheres emerged a slight decrease in the diameter of the microspheres. After reaction for 8 h, the microspheres morphology was irregularly, and the surface of T200 began to be chipped with a disorderly arrangement. In the XRD patterns, it can be seen that the crystallinity of the T200 microspheres increased as the reaction time prolonged.

Figure 10a shows UV–Vis DRS of T200 samples synthesized with different solvothermal reaction time. Distinctly improved optical absorptions in the visible light region could be observed for the resulted T200 microspheres. However, the visible light absorbance was gradually reduced with the increase of reaction time, implying the loss of carbonate species in the prolonged reaction time. From Fig. 10b, it was found the T200 microspheres prepared at 200 °C for 2 h exhibited the best photocatalytic performance. When the reaction time was extended to 8 h, the photocatalytic activity was obviously lowered, which was mainly due to the poor visible light absorbance and the destruction of microsphere structure.

The photocatalytic antibacterial activity of the as-prepared samples was evaluated by the disinfection of *E. coli* under visible light irradiation (Fig. 11). In the light control experiment, the number of *E. coli* cells presented no obvious reduction, suggesting that the effect of visible light to the bacteria could be overlooked. The T400 microspheres displayed low antibacterial efficiency with only 19.1% inactivation of *E. coli* cells after 160 min of visible light illumination. After carbonate species doping, the visible light photocatalytic disinfection activity of T200-4h microspheres was obviously improved as compared with T400 microspheres. When the T200 microspheres were synthesized at 200 °C for 2 h (T200-2h), the disinfection efficiency was further increased, and 80.5% of *E. coli* cells were inactivated over 160 min of visible light exposure. Meanwhile, the mechanism of *E.coli* disinfection was also inspected by the trapping experiments and fluorescent probe technique (Fig. S3). The results revealed that ·OH and $\cdot O_2^-$ played important roles in the inactivation process.

Based on the results described above and previous literatures [16, 20], the possible mechanisms of the enhanced visible-light photocatalytic activity of carbonate-doped TiO_2 microspheres were proposed and shown in Fig. 12. First, the amorphous carbonate doping modified the electronic band structure of TiO_2 and resulted in the formation of VB tail

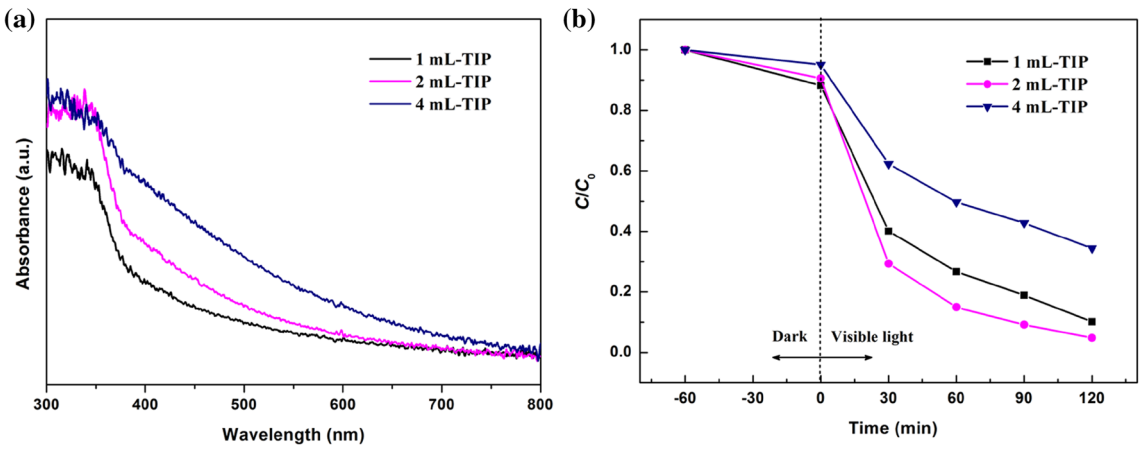

Fig. 8 **a** UV–Vis diffuse reflectance spectra of T200 microspheres prepared with different amount of titanium isopropoxide; **b** photocatalytic degradation of MO over the above samples

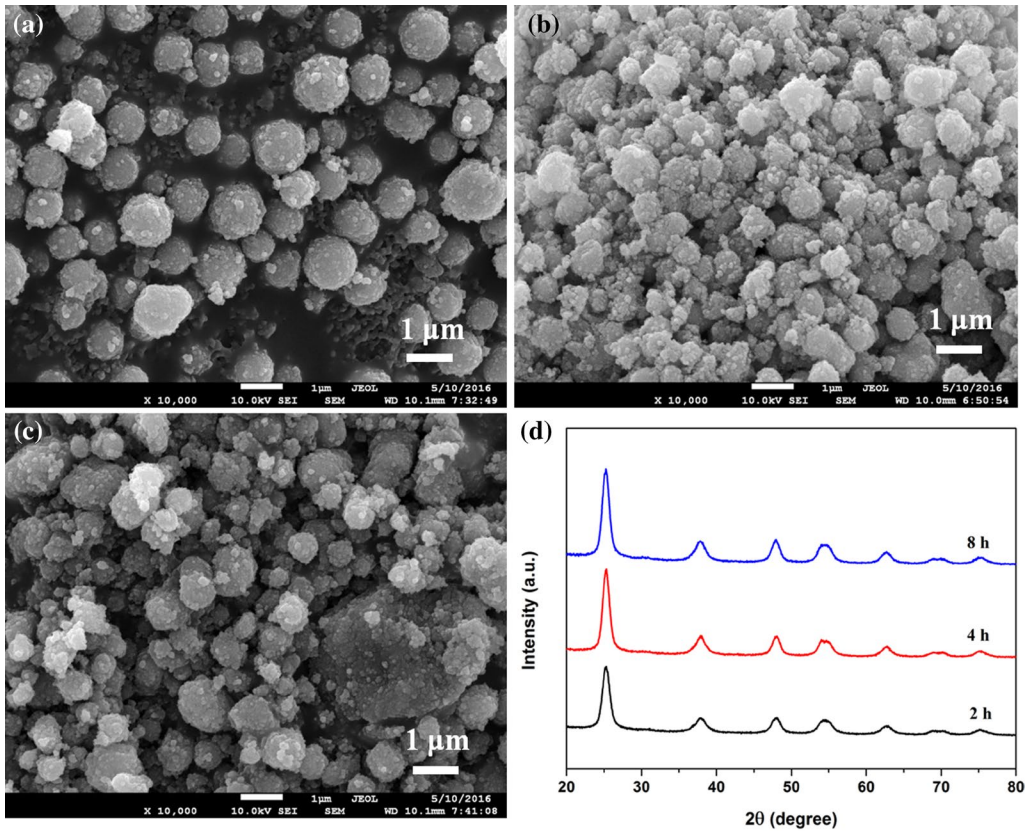

Fig. 9 FESEM images of T200 microspheres prepared at 200 °C for **a** 2 h, **b** 4 h and **c** 8 h; **d** XRD patterns of the above samples

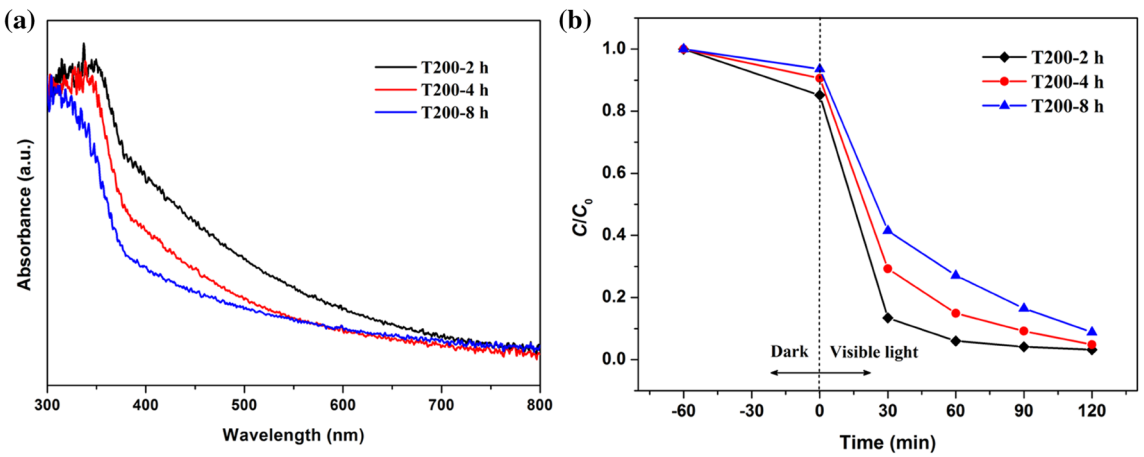

Fig. 10 **a** UV–Vis diffuse reflectance spectra of T200 microspheres prepared at 200 °C for various reaction time; **b** photocatalytic degradation of MO over the above samples

states and bandgap narrowing. Under visible light irradiation, the electrons could be excited directly into the TiO_2 conduction band (CB) and then transferred to the adsorbed O_2 to produce $\cdot O_2^-$. Simultaneously, the photogenerated holes would oxidize the adsorbed H_2O to produce ·OH. On the other hand, the carbonate species on the TiO_2 surface could serve as a photosensitizer for visible light absorption and injected electrons into the CB of TiO_2. The injected electrons could be transferred to the adsorbed O_2 to produce $\cdot O_2^-$. Subsequently, the produced active species (mainly ·OH and $\cdot O_2^-$) participated in the removal of organic pollutants and inactivation of *E. coli* cells. In conclusion, the

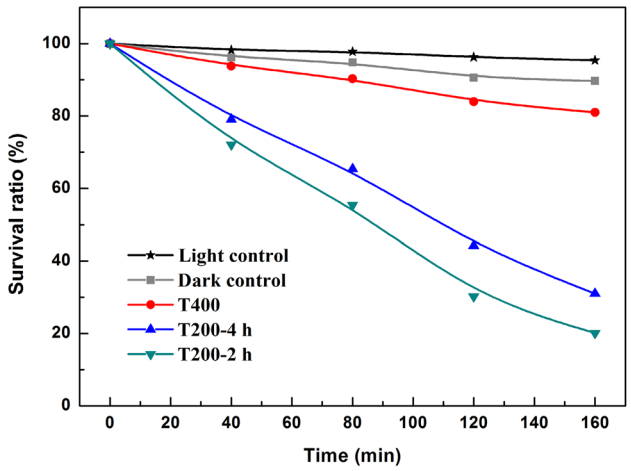

Fig. 11 Photocatalytic disinfection efficiency of *E. coli* for different samples

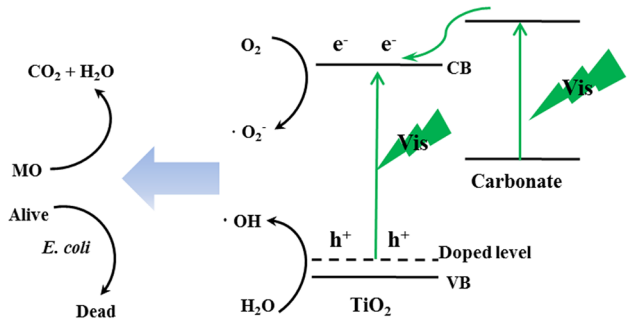

Fig. 12 Schematic diagram of photocatalytic mechanism of carbonate-doped TiO_2 microspheres

carbonate-doped TiO_2 microspheres possessed larger surface area, enhanced visible light absorption and reduced recombination rate of charge carriers, which led to more efficient production of active species and final higher visible light photocatalytic activities.

4 Conclusions

In summary, mesoporous carbonate-doped TiO_2 microspheres were synthesized by a facile solvothermal process and low-temperature annealing process. Compared with non-doped TiO_2 microspheres, the carbonate-doped TiO_2 microspheres exhibited much higher photocatalytic degradation of MO and disinfection of *E. coli* cells under visible light. The improved photocatalytic activities derived from the synergic effects of larger specific surface, stronger visible light absorbance and reduced recombination of electron–hole pairs in the carbonate-doped TiO_2 microspheres. In addition, by adjusting the initial titanium precursor concentration and the reaction time, the morphology, optical and photocatalytic properties of carbonate-doped TiO_2 microspheres could be effectively controllable. This study signifies that the carbonate-doped TiO_2 microspheres would be applied in the water treatment for the degradation of organic pollutants and disinfection of bacteria at the same time.

Acknowledgements The work is financially supported by the National Natural Science Foundation of China (No. 21571160), the National Natural Science Foundation of China-Henan Talents Fostering Joint Funds (No. U1504311), the Key Research Projects of the Science and Technology Department of Henan Province (Nos. 172102210544, 182102210153 and 182102210619), the Fundamental Research Funds for the Provincial Universities (No. 18KYYWF0109) and the Doctoral Scientific Research Foundation of Zhengzhou University of Light Industry (No. 2015BSJJ044).

References

1. H. Tong, S. Ouyang, Y. Bi, N. Umezawa, M. Oshikiri, J. Ye, Adv. Mater. **24**, 229–251 (2012)
2. S. Cao, J. Low, J. Yu, M. Jaroniec, Adv. Mater. **27**, 2150–2176 (2015)
3. H. Yi, D. Huang, L. Qin, G. Zeng, C. Lai, M. Cheng, S. Ye, B. Song, X. Ren, X. Guo, Appl. Catal. B **239**, 408–424 (2018)
4. A. Fujishima, X. Zhang, D.A. Tryk, Surf. Sci. Rep. **63**, 515–582 (2008)
5. K. Nakata, A. Fujishima, J. Photochem, Photobiology C **13**, 169–189 (2012)
6. C. Tang, L. Liu, Y. Li, Z. Bian, Appl. Catal. B **201**, 41–47 (2017)
7. H. Tada, T. Kiyonaga, S. Naya, Chem. Soc. Rev. **38**, 1849–1858 (2009)
8. J. Low, B. Cheng, J. Yu, Appl. Surf. Sci. **392**, 658–686 (2017)
9. S. Rehman, R. Ullah, A.M. Butt, N.D. Gohar, J. Hazard. Mater. **170**, 560–569 (2009)
10. J. Low, J. Yu, M. Jaroniec, S. Wageh, A.A. Al-Ghamdi, Adv. Mater. **29**, 1601694 (2017)
11. J.H. Park, S. Kim, A.J. Bard, Nano Lett. **6**, 24–28 (2006)
12. I. Hiroshi, W. Yuka, H. Kazuhito, Chem. Lett. **32**, 772–773 (2003)
13. Y. Park, W. Kim, H. Park, T. Tachikawa, T. Majima, W. Choi, Appl. Catal. B **91**, 355–361 (2009)
14. S. Sakthivel, H. Kisch, Angew. Chem. Int. Ed. **42**, 4908–4911 (2003)
15. B. Liu, L.-M. Liu, X.-F. Lang, H.-Y. Wang, X.W. Lou, E.S. Aydil, Energy Environ. Sci. **7**, 2592–2597 (2014)
16. J. Liu, L. Han, N. An, L. Xing, H. Ma, L. Cheng, J. Yang, Q. Zhang, Appl. Catal. B **202**, 642–652 (2017)
17. L. Yu, Y. Lin, J. Huang, S. Lin, D. Li, J. Am. Ceram. Soc. **100**, 333–342 (2017)
18. P. Wang, Q. Zhou, Y. Xia, S. Zhan, Y. Li, Appl. Catal. B **225**, 433–444 (2018)
19. F. Liu, X. Yan, X. Chen, L. Tian, Q. Xia, X. Chen, Catal. Today **264**, 243–249 (2016)
20. Y. Wang, A.S. Ganeshraja, C. Jin, K. Zhu, J. Wang, J. Alloys Compd. **765**, 551–559 (2018)
21. B. Liu, L. Mu, B. Han, J. Zhang, H. Shi, Appl. Surf. Sci. **396**, 1596–1603 (2017)
22. Z. Sayyar, A. Akbar Babaluo, J.R. Shahrouzi, Appl. Surf. Sci. **335**, 1–10 (2015)
23. S.M. El-Sheikh, G. Zhang, H.M. El-Hosainy, A.A. Ismail, K.E. O'Shea, P. Falaras, A.G. Kontos, D.D. Dionysiou, J. Hazard. Mater. **280**, 723–733 (2014)

24. Y. Ma, L. Han, H. Ma, J. Wang, J. Liu, L. Cheng, J. Yang, Q. Zhang, Catal. Commun. **95**, 1–5 (2017)
25. I. Corazzari, S. Livraghi, S. Ferrero, E. Giamello, B. Fubini, I. Fenoglio, J. Mater. Chem. **22**, 19105–19112 (2012)
26. D. Gu, Y. Lu, B. Yang, Y.-D. Hu, Chem. Commun. (2008). https://doi.org/10.1039/B800596F
27. B. Liu, Y. Xue, J. Zhang, B. Han, J. Zhang, X. Suo, L. Mu, H. Shi, Environ. Sci. **4**, 255–264 (2017)
28. H. Hou, L. Wang, F. Gao, G. Wei, B. Tang, W. Yang, T. Wu, J. Am. Chem. Soc. **136**, 16716–16719 (2014)
29. X. Ma, Y. Chen, H. Li, X. Cui, Y. Lin, Mater. Res. Bull. **66**, 51–58 (2015)
30. B. Liu, X. Han, Y. Wang, X. Fan, Z. Wang, J. Zhang, H. Shi, J. Mater. Sci. Mater. Electron. **29**, 14300–14310 (2018)
31. H. Wang, Z. Wu, Y. Liu, J. Phys.Chem. C **113**, 13317–13324 (2009)